The Astrophysical Journal, 1003:66 (13pp), 2026 May 20 https://doi.org/10.3847/1538-4357/ae5c97

Resolving the 2024 Outburst of Magnetar 1E 1841-045 from Its Host Supernova Remnant with EP-FXT

Yu-Cong Fu[1,2], Lin Lin[1,2], Yu-Jia Zheng[3,4], Ming-Yu Ge[4,5], Han-Long Peng[3], Dong-Ming Li[1,2], Francesco Coti Zelati[6,7], Ersin Göğüş[8], Nanda Rea[6,7], Bing Zhang[9,10,11,12], Wei-Wei Zhu[1,13], Ke-Jia Lee[13,14,15], Teruaki Enoto[16], and Chryssa Kouveliotou[17,18]

[1] Institute for Frontiers in Astronomy and Astrophysics, Beijing Normal University, Beijing 102206, People's Republic of China; llin@bnu.edu.cn
[2] School of Physics and Astronomy, Beijing Normal University, Beijing 100875, People's Republic of China
[3] School of Physics and Technology, Nanjing Normal University, Nanjing 210023, Jiangsu, People's Republic of China
[4] State Key Laboratory of Particle Astrophysics, Institute of High Energy Physics, Chinese Academy of Sciences, Beijing 100049, People's Republic of China
[5] University of Chinese Academy of Sciences, Chinese Academy of Sciences, Beijing 100049, People's Republic of China
[6] Institute of Space Sciences (ICE, CSIC), Campus UAB, Carrer de Can Magrans s/n, Barcelona E-08193, Spain
[7] Institut d'Estudis Espacials de Catalunya (IEEC), Barcelona E-08034, Spain
[8] Sabanci University, Faculty of Engineering and Natural Sciences, Istanbul 34956, Türkiye
[9] The Hong Kong Institute for Astronomy and Astrophysics, The University of Hong Kong, Pokfulam, Hong Kong, People's Republic of China
[10] Department of Physics, The University of Hong Kong, Pokfulam, Hong Kong, People's Republic of China
[11] Nevada Center for Astrophysics, University of Nevada, Las Vegas, USA
[12] Department of Physics and Astronomy, University of Nevada, Las Vegas, USA
[13] National Astronomical Observatories, Chinese Academy of Sciences, Beijing 100101, People's Republic of China
[14] Department of Astronomy, Peking University, Beijing 100871, People's Republic of China
[15] Kavli Institute for Astronomy and Astrophysics, Peking University, Beijing 100871, People's Republic of China
[16] Department of Physics, Kyoto University, Kyoto 606-8502, Japan
[17] Department of Physics, The George Washington University, Washington, DC 20052, USA
[18] Astronomy, Physics and Statistics Institute of Sciences (APSIS), The George Washington University, Washington, DC 20052, USA
Received 2026 February 5; revised 2026 April 5; accepted 2026 April 6; published 2026 May 14

Abstract

The magnetar 1E 1841–045 exhibited a new active episode starting on 2024 August 20, marked by X-ray bursts and enhanced persistent emission. Using data from the Einstein Probe (EP), we report on the timing and spectral results following the onset of this outburst. The pulse profile displays a multipeaked structure, with notable phase shifts in the secondary peak. Energy-resolved pulse profile analysis indicates a transition in the dominant peak of the pulse profile above 5.8 keV. The 0.5–10 keV X-ray spectrum is well modeled by a combined blackbody and power-law (BB+PL) model, showing a ∼20% flux increase following the outburst. Phase-resolved spectroscopy indicates a correlation between BB temperature and pulse profile intensity, along with spectral hardening at a specific pulse phase. The high spatial resolution of EP enables effective separation of the supernova remnant emission, which is crucial for measuring the intrinsic pulse emission of the source. These findings underscore the intricate relationship between magnetar outbursts, pulse profile evolution, and spectral characteristics.

Unified Astronomy Thesaurus concepts: Neutron stars (1108); Magnetars (992); X-ray transient sources (1852)

1. Introduction

Magnetars are a unique class of isolated neutron stars (NSs) whose X-ray emissions, including persistent emission and X-ray bursts, are mainly powered by their extremely intense magnetic fields (e.g., R. C. Duncan & C. Thompson 1992; C. Thompson & R. C. Duncan 1993; C. Kouveliotou et al. 1998). The magnetic fields are estimated from their spin periods P (within a range of ∼1–12 s) and spin-down rates $\dot{P}$ (within a range of $\sim 10^{-13}$–10^{-10} s s^{-1}), mainly exceeding $\sim 10^{14}$ G[19] (S. A. Olausen & V. M. Kaspi 2014). During the active period of magnetars, the brightening of persistent X-ray emission is frequently accompanied by short X-ray bursts, often along with the variation in spectral and timing properties (e.g., P. M. Woods et al. 2004; G. Younes et al. 2017a; Y.-C. Fu et al. 2025; N. Rea & D. De Grandis 2026).

The soft X-ray emission observed in magnetars is predominantly attributed to NS surface emission, which is modified by the resonant scattering processes occurring within the magnetosphere (e.g., C. Thompson et al. 2002; M. Lyutikov & F. P. Gavriil 2006; H. Tong et al. 2010). The persistent X-ray spectra below 10 keV typically require two components, commonly well described by either an absorbed blackbody plus power-law (BB+PL) model or an absorbed double blackbody (BB+BB) model. These models are characterized by a typical BB temperature ($kT_{\rm BB}$) of ∼0.5 keV and a photon index of ∼2–4 in the BB+PL case or by two distinct thermal components, with the cooler BB at $kT_{\rm cool} \sim 0.3$ keV and the hotter BB at $kT_{\rm hot} \sim 0.7$ keV in the BB+BB case (S. A. Olausen & V. M. Kaspi 2014; S. Mereghetti et al. 2015). During magnetar outbursts, the spectral evolution accompanying the decay in luminosity is often distinctive, characterized by phenomena such as spectral hardening and an increase in the inferred surface temperature (F. Coti Zelati et al. 2018). Additionally, temporal properties may also exhibit concurrent changes, including the occurrence of glitches/antiglitches and

[19] Refer to the online McGill SGR/AXP catalog, which contains the current information available on 30 magnetars, at: http://www.physics.mcgill.ca/~pulsar/magnetar/main.html.

the variation in the pulse profile (e.g., R. F. Archibald et al. 2013; G. Younes et al. 2017b; M.-Y. Ge et al. 2024; Y.-C. Fu et al. 2025).

1E 1841–045, initially discovered in 1985, is located at the center of the supernova remnant (SNR) Kes 73 (or G27.4+0.0, G. A. Kriss et al. 1985). It was later identified as a pulsar in 1997 through the detection of its spin period (G. Vasisht & E. V. Gotthelf 1997). The spin period of 1E 1841–045 was calculated as $P \sim 11.8$ s, with a spin-down rate of $\dot{P} \sim 4 \times 10^{-11}$s s^{-1}, which implies a dipolar magnetic field strength of $B \sim 7 \times 10^{14}$ G (G. Vasisht & E. V. Gotthelf 1997; E. V. Gotthelf et al. 1999). The source is located at a distance initially estimated as $8.5^{+1.3}_{-1.0}$ kpc from the H I/II absorption and emission of Kes 73 (W. W. Tian & D. A. Leahy 2008), which has been updated to 5.8 ± 0.3 kpc from the reanalysis of H I absorption features (S. Ranasinghe & D. A. Leahy 2018). Over several decades, 1E 1841–045 has experienced occasional X-ray bursts, but its persistent soft X-ray emission has maintained a nearly constant luminosity (e.g., E. V. Gotthelf et al. 1999; W. Zhu & V. M. Kaspi 2010; L. Lin et al. 2011; H. An et al. 2015). Additionally, persistent hard X-ray emission in the range of 15–200 keV has been detected, characterized by a PL photon index of 1.3 (e.g., L. Kuiper et al. 2004; H. An et al. 2013, 2015).

Deep radio observations of the magnetar 1E 1841–045 were conducted in previous studies. The Parkes radio telescope (1.4 GHz; M. Burgay et al. 2006), Green Bank Telescope (GBT, 1950 MHz; P. Lazarus et al. 2012), Five-hundred-meter Aperture Spherical radio Telescope (FAST, 1250 MHz; J. Bai et al. 2025), MeerKAT (*L*-band and *S*-band), and Effelsberg radio telescopes (1.3–6.0 GHz; G. Younes et al. 2025) have yielded no detections of pulsed or single-pulse radio emission. The consistent lack of detections, despite using multiple sensitive telescopes across a range of frequencies, strongly suggests the source is radio quiet.

On 2024 August 20, 1E 1841–045 entered a new active period, triggering several instruments with a series of short bursts. Swift/BAT detected four bursts within the 15–350 keV energy range on August 20 and 21 (J. J. DeLaunay et al. 2024; S. Dichiara et al. 2024). Fermi/GBM also recorded eight bursts from this source between August 20 and 22, three of which were temporally coincident with Swift's detections (O. J. Roberts et al. 2024). Additionally, burst activity was reported by SVOM/GRM (SVOM/GRM Team et al. 2024a, 2024b), GECAM (W.-L. Zhang et al. 2024), INTEGRAL (S. Mereghetti et al. 2024), NICER (M. Ng et al. 2024), and Insight-HXMT (C. Cai et al. 2024). Notably, NICER observations revealed a ∼25% increase in the persistent emission flux in the 0.5–10 keV range, along with a change in the structure of the pulse profile compared to the preburst (August 3) level (M. Ng et al. 2024; G. Younes et al. 2024).

During its 2024 active period, IXPE observations of 1E 1841–045 revealed a highly polarized X-ray emission, whose polarization degree (PD) changed from ∼15% at 2–3 keV to ∼55% at 6–8 keV (M. Rigoselli et al. 2025; R. Stewart et al. 2025). The 2–79 keV broadband spectrum was well modeled by a combination of a BB and two PL components, with the hard PL component suggesting a synchrotron/curvature origin. The soft PL component was thought to be the emission from a Comptonized corona in the inner magnetosphere (R. Stewart et al. 2025). Following a spin-up glitch detection, NICER and NuSTAR observed a narrow peak in the pulse profile gradually moving closer to the main peak (G. Younes et al. 2025).

In this study, we report the results of target-of-opportunity (ToO) multiwavelength observations of 1E 1841–045, carried out with the Einstein Probe (EP) and FAST. The details of the observations and data reduction are provided in Section 2, the data analysis and results are described in Section 3, and the discussion and conclusions are given in Section 4.

2. Observations and Data Reduction

2.1. X-Ray Observations

The EP, launched on 2024 January 9, is a mission led by the Chinese Academy of Sciences (W. Yuan et al. 2022, 2025). Focused on time-domain high-energy astrophysics, EP is equipped with two instruments: the Wide-field X-ray Telescope (WXT) and the Follow-up X-ray Telescope (FXT). EP/WXT,[20] a soft X-ray focusing telescope (0.5–4 keV), employs an exceptionally wide instantaneous field of view (FOV), covering 3600 square degrees, combined with a moderate spatial resolution of ∼5′ (full width at half-maximum) and a time resolution of ∼50 ms (Y.-H. I. Yin et al. 2024; Y. Liu et al. 2025; W. Zhang et al. 2025). EP/FXT,[21] a Wolter-I telescope operating in the 0.5–10 keV energy range, employs a narrow FOV with a diameter of 60′ and a source localization error of 5″–15″ (Y. Chen et al 2020). Consisting of two coaligned identical units, FXT-A and FXT-B, FXT supports three scientific observation modes: full-frame mode (FF, time resolution of 50 ms), partial-window mode (PW, time resolution of 2.2 ms), and timing mode (TM, time resolution of 23.68 μs). Its primary role is to perform rapid follow-up observations (within 5 minutes) of the sources triggered by WXT, and will also observe other interesting targets during the all-sky survey.

Following the detection of the burst activity, FXT conducted the ToO observations of 1E 1841–045 from 2024 August 22 to September 29, accumulating a total net exposure time of ∼85 ks. Additionally, FXT also observed the source during its Cycle-1 proposal before bursts (on 2024 July 14) with a net exposure time of ∼900 s. The observational details of FXT are summarized in Table 1. During the all-sky monitoring, WXT covered the sky region containing the source and identified it in a total of 206 observations from 2024 May 17 to September 29. The WXT observed flux[22] within the 0.5–4 keV range exhibits fluctuations ranging from 0.6 to 4.5, having an average value of 1.88 and a standard deviation of 0.61 (in units of 10^{-11} erg s^{-1} cm^{-2}). Subsequently, 1E 1841–045 became invisible due to a solar aspect angle smaller than 94.°5. The time intervals of WXT and FXT observations are illustrated in Figure 1.

We processed the WXT observations using `wxtpipeline`, a dedicated analysis toolchain within the WXT data analysis software (WXTDAS[23]) and the calibration database (CALDB), both developed by the EP Science Center (EPSC). Applying the default calibration and screening procedures of `wxtpipeline`, we extracted the source light curves and spectra from a circular region with a radius of 300.″0 to obtain

[20] https://ep.bao.ac.cn/ep/cms/article/view?id=39
[21] http://epfxt.ihep.ac.cn/about
[22] https://ep.bao.ac.cn/ep/data_center/wxt_observation_data
[23] https://ep.bao.ac.cn/ep/cms/article/view?id=182

Table 1
EP/FXT Observations of 1E 1841–045

Obs. ID	Time (MJD)	Date (UTC)	Exp[a] (s)	Mode	Rate[b] (cts s^{-1})	Flux[c] (10^{-11})	kT_{BB} (keV)	Γ
11908432129	60505.57	2024-7-14	936	FF	1.05 ± 0.04	4.94 ± 0.17	0.47 ± 0.03	1.90[d]
06800000053	60544.74	2024-8-22	9009	FF	1.25 ± 0.01	6.36 ± 0.06	0.46 ± 0.02	$1.99^{+0.10}_{-0.11}$
10202120449	60551.49	2024-8-29	2752	FF	1.21 ± 0.02	5.88 ± 0.11	0.45 ± 0.02	$1.85^{+0.21}_{-0.25}$
06800000059	60552.62	2024-8-30	8967	PW	1.19 ± 0.01	5.67 ± 0.06	0.48 ± 0.01	$1.80^{+0.12}_{-0.13}$
06800000060	60553.62	2024-8-31	1402	PW	1.14 ± 0.03	5.47 ± 0.15	0.52 ± 0.05	$1.87^{+0.28}_{-0.48}$
06800000061	60554.49	2024-9-01	8958	PW	1.19 ± 0.01	5.89 ± 0.06	0.50 ± 0.02	$1.99^{+0.09}_{-0.11}$
06800000063	60555.67	2024-9-02	8952	PW	1.20 ± 0.01	5.73 ± 0.06	0.47 ± 0.01	$1.78^{+0.14}_{-0.16}$
06800000068	60556.50	2024-9-03	8951	PW	1.19 ± 0.01	5.58 ± 0.06	0.47 ± 0.01	$1.60^{+0.14}_{-0.16}$
06800000067	60557.43	2024-9-04	5965	PW	1.16 ± 0.01	5.30 ± 0.07	0.48 ± 0.01	$1.34^{+0.25}_{-0.29}$
06800000071	60558.43	2024-9-05	2982	PW	1.20 ± 0.02	6.04 ± 0.06	0.51 ± 0.02	$2.06^{+0.09}_{-0.10}$
06800000069	60558.63	2024-9-05	8949	PW	1.20 ± 0.01	6.26 ± 0.11	0.50 ± 0.03	$2.15^{+0.14}_{-0.17}$
06800000070	60559.77	2024-9-06	5966	PW	1.19 ± 0.01	6.27 ± 0.08	0.51 ± 0.03	$2.13^{+0.09}_{-0.11}$
06800000072	60560.64	2024-9-07	2983	PW	1.22 ± 0.02	5.93 ± 0.11	0.46 ± 0.02	$1.80^{+0.22}_{-0.27}$
06800000076	60561.64	2024-9-08	2984	PW	1.22 ± 0.02	5.59 ± 0.10	0.46 ± 0.01	$1.49^{+0.24}_{-0.28}$
08500000151	60582.42	2024-9-29	5799	PW	1.18 ± 0.02	6.34 ± 0.08	0.48 ± 0.02	$2.24^{+0.09}_{-0.11}$

Notes.
[a] Net exposure time (s) for each observation.
[b] The 0.5–10 keV net count rate of FXT-A and FXT-B.
[c] The 0.5–10 keV unabsorbed flux in units of 10^{-11} erg s^{-1} cm^{-2}.
[d] The fixed parameter.

as many source photons as possible. The FXT observations were processed with the `fxtchain` tool, which is a part of the FXT data analysis software (FXTDAS,[24] v1.10) developed by the EPSC. Using the CALDB v1.10 and the default parameters, we extracted the clean event files, Good Time Interval (GTI) files, and image files. As shown in Figure 2, the source region was defined as a circular area with a radius of 30.″0. The background region, which is located within the SNR, was selected from an annulus with the inner and outer radii of 40.″0 and 100.″0, respectively. Finally, the light curves and spectra were extracted using XSELECT v2.5b.

The events of the source region in the energy range of 0.5–4 keV (WXT) and 0.5–10 keV (FXT) after the barycenter correction were used for timing analysis. We used the epoch folding method (D. A. Leahy 1987) to determine the initial period of the NS (e.g., A. Borghese et al. 2020; Y.-C. Fu et al. 2023, 2025), and used the TEMPO2 (R. T. Edwards et al. 2006) v2024.12.1 to update the more accurate ephemeris of the source. Times of arrival (ToAs) were derived through Z^2 searching, with the minimum phase in each profile serving as the ToA for the corresponding observation (M. Y. Ge et al. 2012, 2019; G. Younes et al. 2020; H.-L. Peng et al. 2026). For spectral analysis, we performed fitting using XSPEC (K. A. Arnaud 1996) v12.14.1, as part of HEASoft v6.34, which allowed us to model and analyze the spectra comprehensively.

NICER data that partly overlap in time with the FXT observations are used to supplement the FXT timing dataset. Standard processing, including the creation of cleaned and calibrated event files, is performed using the `nicerl2` tool within NICERDAS v12. Further details and results of the NICER data processing are provided by G. Younes et al. (2025).

[24] http://epfxt.ihep.ac.cn/analysis

2.2. Radio Observations

The radio observations were carried out with the highly sensitive FAST telescope (P. Jiang et al. 2020). Following the X-ray activity, we conducted coordinated radio and X-ray observations of 1E 1841–045 using FAST and EP/FXT, respectively (see Figure 1). From 2024 August to September, we obtained seven FAST observations totaling 5.14 hr, with individual sessions typically lasting 30–60 minutes, as shown in Table 2. These observations covered the 1–1.5 GHz band with high sensitivity, utilizing a setup of 4096 channels (0.122 MHz $channel^{-1}$) and a time resolution of 49.152 μs.

3. Results

3.1. The Joint Observations and EP Burst Search

After the onset of the 2024 August 20 active episode, multiple telescopes conducted follow-up observations. The observation timelines for EP, Insight-HXMT, NICER, Swift/XRT, and FAST are summarized in Figure 1. A notable coordinated multiwavelength observation involving FAST and EP was performed simultaneously around MJD 60582.5.

We apply a Poissonian procedure to search for potential X-ray bursts for EP (e.g., F. P. Gavriil et al. 2004). The initial light curves from EP/WXT are extracted with time resolutions of 0.05, 0.1, 0.2, and 0.5 s. No significant signals exceeding the 3σ threshold are detected. Additionally, no X-ray bursts were identified in the blind search of the EP/FXT data, with the significance of any candidate event failing to exceed the 3σ threshold above the persistent emission. Compared with the reported bursts (C. Cai et al. 2024; S. Dichiara et al. 2024; SVOM/GRM Team et al. 2024a, 2024b; M. Ng et al. 2024; O. J. Roberts et al. 2024) shown in Figure 1, the EP observations missed the most active epoch of bursts.

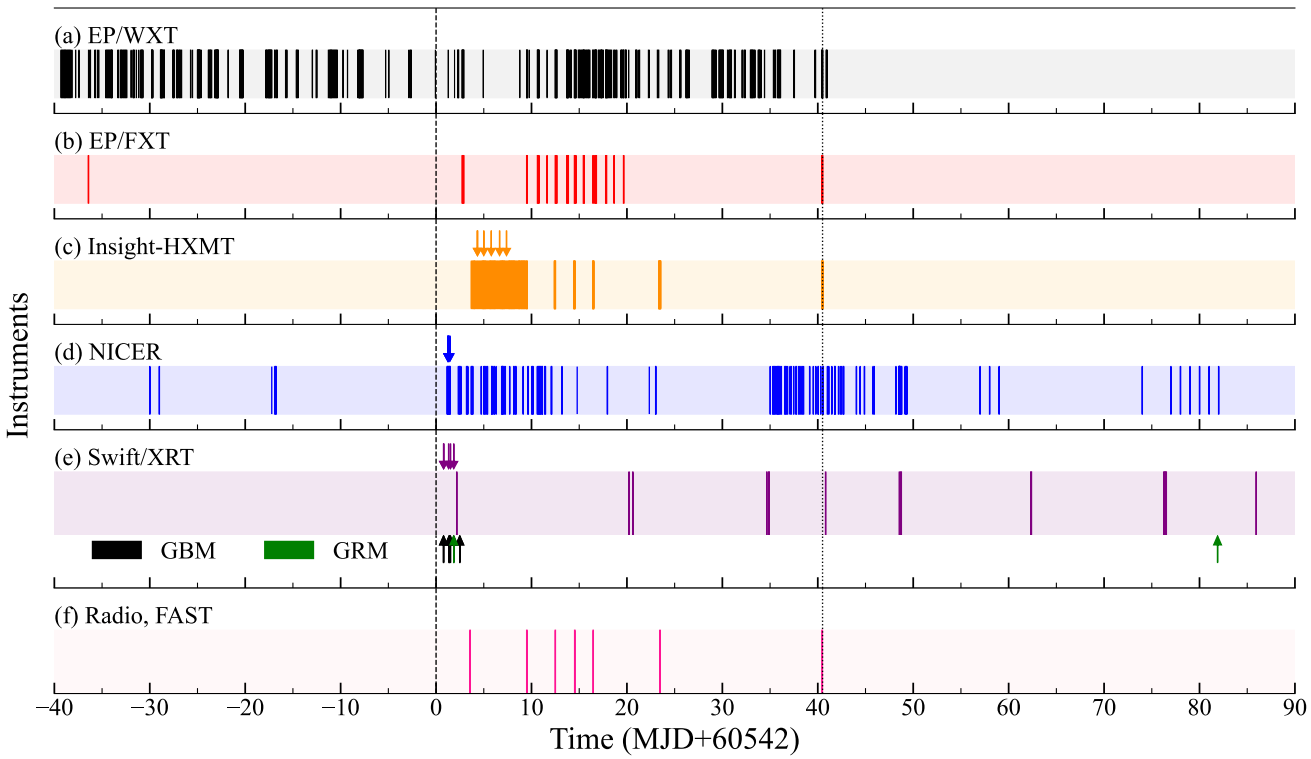

Figure 1. Observation timelines for different instruments. The dark vertical bars in each panel indicate the observation epochs. The arrows mark the time of the short bursts reported in the references. In panel (e), the purple arrows correspond to bursts detected by Swift/BAT, while the black and green arrows represent the bursts detected by Fermi/GBM and SVOM/GRM, respectively. The dashed and dotted vertical lines represent the onset of the outburst and the epoch of a joint FAST and EP observation, respectively.

3.2. Timing Analysis

The statistical sample of the WXT events is insufficient to yield significant timing results. In contrast, the periods detected by FXT exhibit high significance, with the optimal spin frequency f and its derivative $\dot{f}$ determined to be 0.084699549(8) Hz and $-2.49(6) \times 10^{-13}$ Hz s^{-1}, respectively, at a reference epoch of MJD 60549. The ephemeris derived from FXT data is consistent with the results obtained from NICER data (G. Younes et al. 2025). To improve statistical analysis, we combine the FXT and NICER observations during the same time interval. As detailed in Table 3, the best fit to the FXT and NICER data spanning MJD 60505 to MJD 60584 yields a spin frequency f and its derivative $\dot{f}$ of 0.084699564(6) Hz and $-3.04(5) \times 10^{-13}$ Hz s^{-1}, respectively. The resulting fit yields a reduced chi-square (χ^2/dof) of 43.54/34 (∼1.28), which is an improvement over the value of 24.24/17 (∼1.43) from the FXT data alone.

3.2.1. Pulse Profiles

The average pulse profiles before and after the outburst in the 0.5–10 keV band, compared in Figure 3, show significant variability. Epoch I represents the pulse profile before the outburst, associated with Obs. ID 11908432129 on MJD 60505.57. Epoch II represents the average pulse profile following the outburst, spanning from MJD 60544.74 to MJD 60582.45. The phase alignment between epoch I and epoch II is achieved by maximizing the Pearson correlation coefficient through circular shifting of the pulse profiles. The preoutburst profile exhibits a double-peaked structure. Following the outburst, this is replaced by a multipeaked structure.

The FXT pulse profiles during epoch II display a multipeaked structure within the 0.5–10 keV energy range, featuring peak I at approximately phase 0.9, peak II at phase 0.2, and peak III at phase 0.5, as shown in Figure 4. The colors representing the values of the pulse profile are normalized by the pulse/average count rate; the red represents the pulse-on phase, and the blue represents the pulse-off phase. The phase and shape of peak II (the main peak) remain relatively stable, while peaks I and III exhibit a rightward phase shift. Over the 38 day epoch from MJD 60544 to MJD 60582, the phase-shift of peak I is ∼0.1 cycles, corresponding to a rate of $\sim 2.6 \times 10^{-3}$ cycles day^{-1}, consistent with the findings reported by G. Younes et al. (2025). However, the significant fluctuations in the phase of peak I do not support obtaining a robust quantification through linear fitting. Peak III appears to follow a similar trend to peak I, but its lower intensity causes it to intermittently appear and disappear. Thus, the apparent broadening of peak III to the right in Figure 4 is more likely to be caused by a reduced signal-to-noise ratio rather than a definitive phase shift.

3.2.2. Energy-resolved Pulse Profile

The pulse profile demonstrates a variability across different energy bands. As illustrated in Figure 5, the full energy range of the FXT (0.5–10 keV) is segmented into seven intervals. To ensure sufficient counting statistics in each energy interval, from the top to the bottom panels, the seven energy bands correspond to 0.5–1.8 keV, 1.8–2.3 keV, 2.3–3.3 keV, 3.3–4.3 keV, 4.3–5.8 keV, 5.8–7.5 keV, and 7.5–10 keV, respectively.

The triple-peaked phase structure remains relatively stable across the 0.5–10 keV energy range, with no evidence for significant phase change. The normalized intensities of peaks I

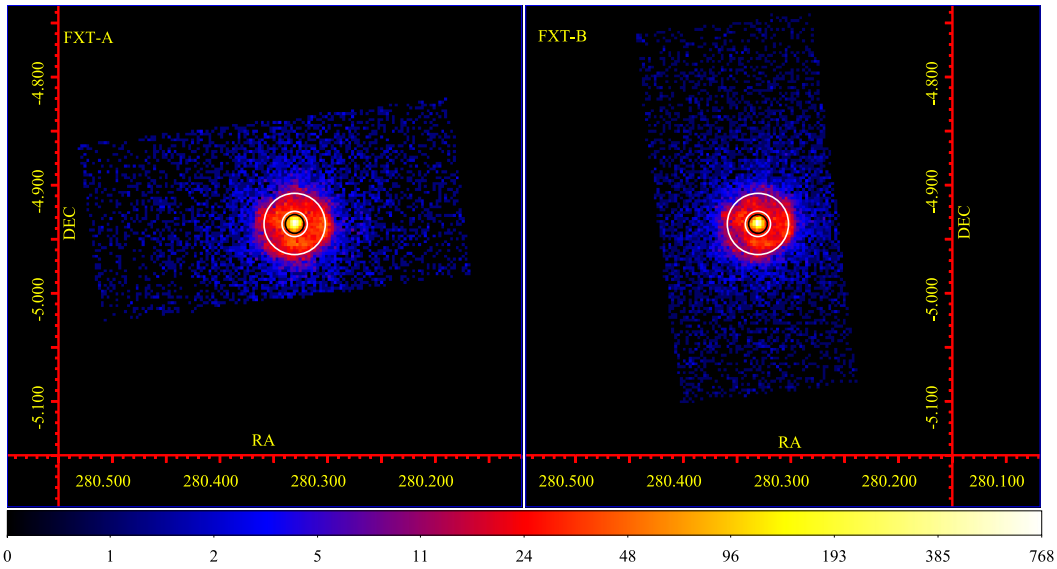

Figure 2. Logarithmic scale images of 1E 1841–045 captured by FXT-A (left) and FXT-B (right) of Obs. ID 06800000059 (MJD 60552.62). The blue rectangular areas indicate the FXT fields of view in PW mode. A black circle with a 30″ radius displays the central source. A white annulus with a 40″ inner radius and a 100″ outer radius displays the surrounding SNR. The color bar shows the counts per pixel.

Table 2
FAST Observations of 1E 1841–045

Observation Date (YYYYMMDD)	Start Time (MJD)	Exposure (minutes)
20240823	60545.553	38
20240829	60551.492	60
20240901	60554.487	30
20240903	60556.517	60
20240905	60558.458	30
20240912	60565.458	30
20240929	60582.444	60

Table 3
Best-fit Spin Parameters of 1E 1841–045 from EP/FXT and NICER Data

Parameter	FXT and NICER	FXT
R.A. (J2000)	18:41:19.6	
Decl. (J2000)	−04:56:07.4	
Start (MJD)	60505	
Finish (MJD)	60584	
Reference epoch (MJD)	60549	
Spin frequency f (Hz)	0.084699564(6)	0.084699549(8)
Spin-down rate $\dot{f}$ (10^{-13} Hz s^{-1})	−3.04(5)	−2.49(6)
χ^2/dof	43.54/34	24.24/17

and II remain approximately constant at ∼1.1 and ∼1.2, respectively.

Peak III, however, displays distinct behavior: it persists as a minor peak with modest fluctuations below 5.8 keV, though it nearly vanishes transiently at 1.8–2.3 keV. Above 5.8 keV, it undergoes marked enhancement, exhibiting a clear tendency to exceed the intensity of the main peak.

3.2.3. Pulsed Fraction

We further investigated the evolution of the pulsed fraction (PF) as a function of both time and energy. After carefully

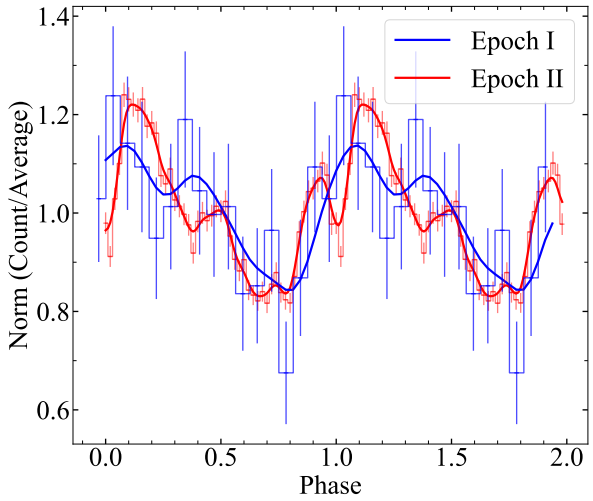

Figure 3. The average pulse profiles of 1E 1841–045 during two epochs observed by FXT in the 0.5–10 keV band. Epoch I represents the pulse profile before the outburst, corresponding to Obs. ID 11908432129 on MJD 60505.57. Epoch II represents the average pulse profile after the outburst, spanning from MJD 60544.74 to MJD 60582.45. The phase of epoch I is aligned to epoch II using circular cross-correlation. The solid lines represent the smoothed pulse profiles after Gaussian filtering.

accounting for and subtracting the contribution from the surrounding SNR, we calculated the PF. Specifically, to isolate the magnetar's emission, we folded the SNR data using the magnetar's timing ephemeris to produce a background profile. Subsequently, after scaling the SNR background counts to account for the different sizes of the extraction areas,[25] we subtracted the background pulse profile from the magnetar's. This enabled us to isolate the magnetar's intrinsic pulse profile and, consequently, obtain its intrinsic PF from the following

[25] $C_{\mathrm{SNR,\,scaled}} = C_{\mathrm{SNR,\,extracted}} \times \frac{A_{\mathrm{src}}}{A_{\mathrm{SNR}}}$, where $C_{\mathrm{SNR,\,extracted}}$ is the background counts from the SNR region, and A_{src} (A_{SNR}) is the area of the source (background) extraction region.

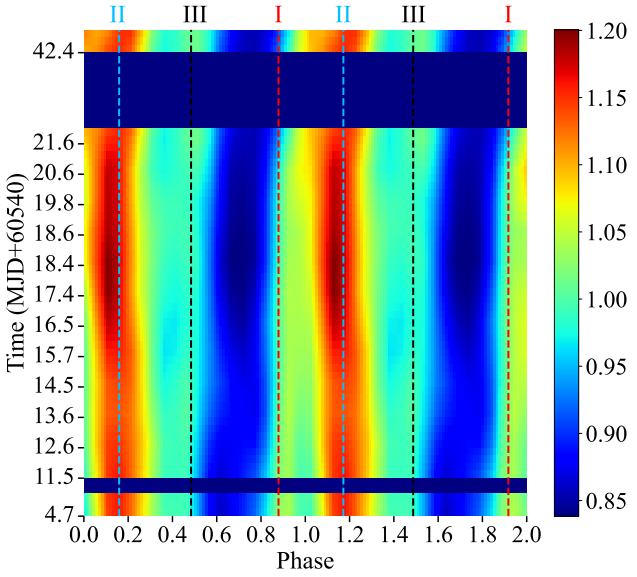

Figure 4. The two-dimensional (2D) map illustrates the evolution of the pulse profiles over time for FXT (0.5–10 keV) from MJD 60544.74 to MJD 60582.45 (epoch II in Figure 3). The colors represent the normalized values of the pulse profile, where normalization is based on the pulse/average count rate. To create the map, 20 bins within a phase are used to fold the pulse profiles. For clarity, the plot is further smoothed through interpolation and Gaussian filtering.

expression:

$$PF = \frac{I_{\max} - I_{\min}}{I_{\max} + I_{\min}}, \quad (1)$$

where $I_{\max}$ and $I_{\min}$ represent the maximum and minimum intensities of the intrinsic pulse profile, respectively.

As shown in Figure 6(a), the temporal evolution analysis reveals that the PF remains remarkably stable at 23.4 ± 2.9% throughout the observation period, showing no significant variations. The energy-dependent behavior of the PF is shown in Figure 6(b). We first performed a weighted linear fit: PF (%) = 2.8(9) × E(keV) + 14(3), with $\chi^2/\nu = 1.98/5$. The red shaded area represents the 1σ confidence interval. The uncertainty of the weighted regression was quantified using Gaussian error propagation. The slope of the fit remains statistically significant ($t(5) = 3.1$, $p < 0.05$), indicating a positive trend across the entire energy range. However, the widening of the confidence interval above 5.8 keV suggests that this overall trend is predominantly constrained by the low-energy points, while the high-energy behavior remains poorly constrained. We further performed a broken-line fit, which yields a turning point at $x_0 = 6.9 \pm 2.2$ keV with $y_0 = 33.8\% \pm 4.2\%$:

$$\mathrm{PF}(\%) = \begin{cases} 14.1 + 2.9(1.5) \times E \quad (\mathrm{keV}), & E < 6.9\ \mathrm{keV} \\ 33.8 + 0.0(0.7) \times E \quad (\mathrm{keV}), & E \geqslant 6.9\ \mathrm{keV} \end{cases}, \quad (2)$$

where the values in parentheses represent the 1σ uncertainties of the fitted parameters. The positive slope in the first segment ($E < 6.9$ keV) is marginally significant, while the slope in the second segment ($E \geqslant 6.9$ keV) is consistent with zero, indicating a plateau after the turning point. The fit yields $\chi^2/\nu = 1.89/3$, confirming a good description of the data. The F-test shows no significant improvement of the broken-line model over the linear model ($P = 0.93 > 0.05$).

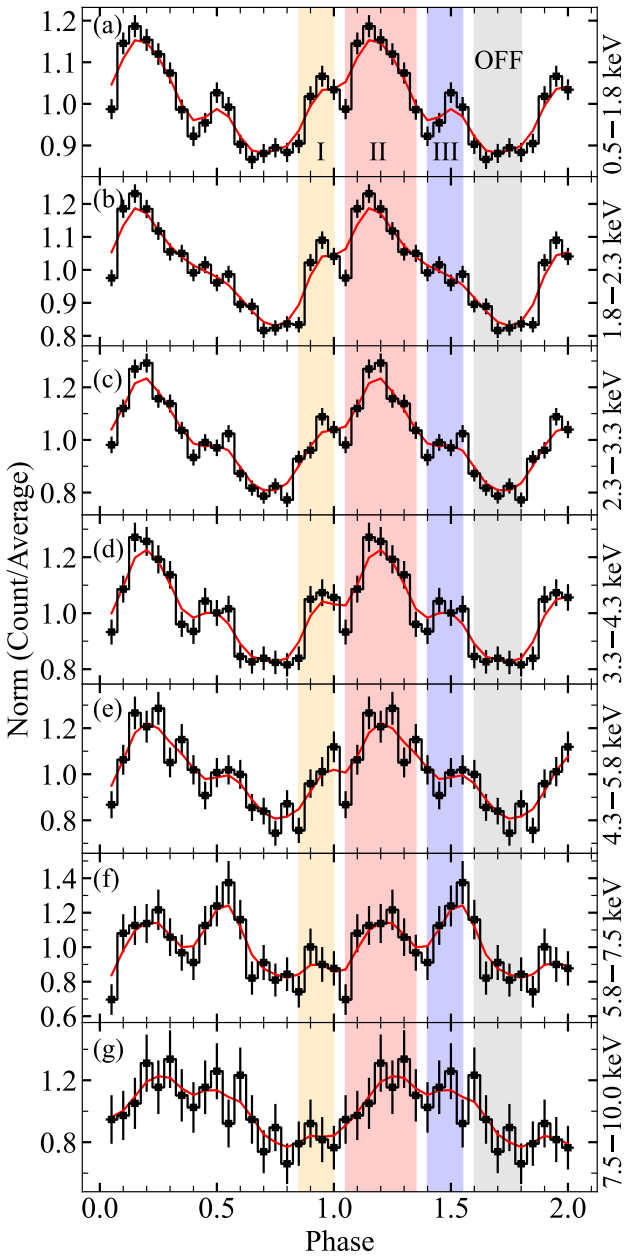

Figure 5. The evolution of the pulse profiles over energy for FXT (0.5–10 keV). The values of the pulse profiles are normalized by the pulse/average count rate, generated from the combined data spanning from MJD 60544.74 to MJD 60582.45 (epoch II in Figure 3). The seven panels, from top to bottom, correspond to the energy bands of 0.5–1.8 keV, 1.8–2.3 keV, 2.3–3.3 keV, 3.3–4.3 keV, 4.3–5.8 keV, 5.8–7.5 keV, and 7.5–10 keV, respectively. The red lines in each panel represent the smoothed pulse profiles after Gaussian filtering. The orange, red, blue, and gray shaded areas correspond to the phase intervals of peak I, II, III, and the pulse-off period, respectively.

3.3. Spectral Analysis

We extracted the source and background spectra following the region selection criteria detailed in Section 2 (Figure 2). The spectra were grouped to have at least five counts per bin for the fit to enable a reliable C-statistic. The goodness of the fit was subsequently evaluated using the χ^2 statistic.

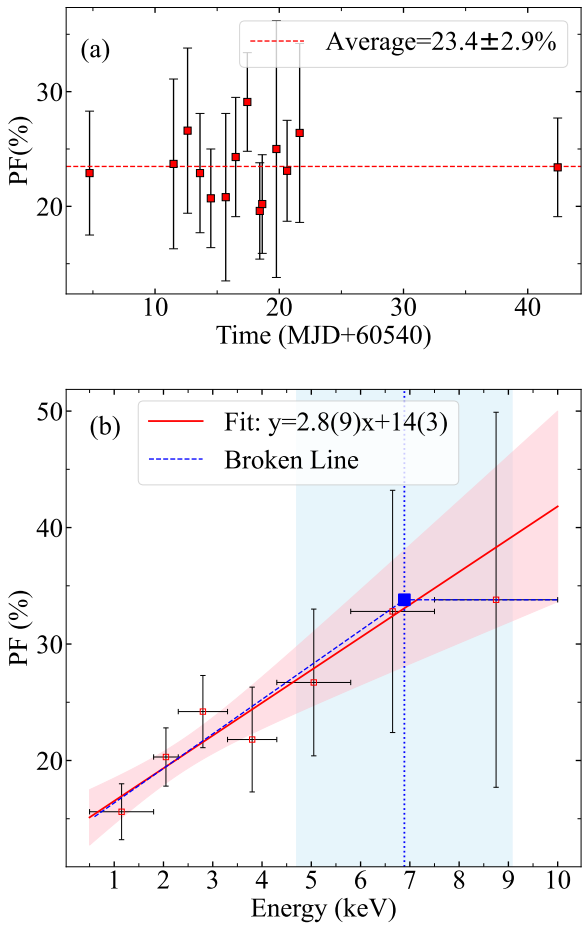

Figure 6. The evolution of the pulsed fraction (PF) of 1E 1841–045. (a) The evolution of PF over time, with the red dashed line representing the average value. (b) The evolution of PF over energy. The horizontal error bars denote the energy bin widths, with each point plotted at the bin centroid. The red solid line shows the weighted linear fit, with the red shaded area representing the 1σ statistical uncertainties. The blue dashed line shows the broken-line model fit. The blue vertical dotted line and the shaded region mark the turning point at $x_0 = 6.9 \pm 2.2$ keV and its 1σ uncertainty.

As shown in Figure 7(a), the spectra of FXT-A and FXT-B were jointly modeled well using an absorbed BB+PL model.[26] In the joint spectral fits, the cross-normalization constant between FXT-A and FXT-B was fixed at 1, as their calibrations are known to be consistent across the employed energy band. The source radius in kilometers is calculated from the distance of 8.5 kpc (W. W. Tian & D. A. Leahy 2008). According to the joint fitting of all FXT observations, the typical parameters for the absorbed BB+PL model are as follows: the hydrogen column density ($N_{\rm H}$) is $(2.08 \pm 0.06) \times 10^{22}\,{\rm cm}^{-2}$, the BB temperature ($kT_{\rm BB}$) is 0.50 ± 0.01 keV, the BB radius is 6.08 ± 0.12 km, and the PL photon index is 1.91 ± 0.13. The fit yields $\chi^2/{\rm dof} = 754/691 \approx 1.09$, indicating a good description of the data. In the spectral evolution and phase-resolved analysis, we fix $N_{\rm H}$ to $2.08 \times 10^{22}\,{\rm cm}^{-2}$ to reduce the impact of statistical fluctuations. The fitting results demonstrate that with degrees of freedom ranging from 296 to 794, the $\chi^2/{\rm dof}$ for all observations ranged from 0.98 to 1.09.

Additionally, the double blackbody model[27] is also applicable to the spectra of the source, as shown in Figure 7(b). The typical parameters for the absorbed BB+BB model are as follows: the $N_{\rm H}$ is $(1.73 \pm 0.03) \times 10^{22}\,{\rm cm}^{-2}$, the cooler BB temperature ($kT_{\rm cool}$) is 0.57 ± 0.01 keV, the cooler BB radius is 6.07 ± 0.08 km, the hotter BB temperature ($kT_{\rm hot}$) is 2.21 ± 0.08 keV, and the hotter BB radius is 0.36 ± 0.06 km. The fit yields $\chi^2/{\rm dof} = 803/691 \approx 1.16$, indicating an acceptable description of the data. Compared to the BB+BB model, the BB+PL model provides a marginally better fit (an improvement of about 6% in χ^2). In the phase-resolved analysis, we fix the $N_{\rm H}$ of the BB+BB model to $1.73 \times 10^{22}\,{\rm cm}^{-2}$ to reduce the impact of statistical fluctuations.

We also attempted to include an additional PL component to investigate the impact of the hard PL on the soft PL (or hotter BB) component. To do so, we fitted the averaged spectra using both a BB+PL+PL and a BB+BB+PL model. The parameters of the hard PL component proved extremely difficult to constrain. Even with the $N_{\rm H}$ and $kT_{\rm BB}$ fixed, the fitting only provided upper limits of 8.5 and 9.2 for the photon index of the hard PL in the two models, respectively. The F-test yielded p-values of 0.17 and 0.075 ($P > 0.05$) for the two cases, respectively, indicating that the inclusion of the hard PL component did not significantly improve the goodness of fit. To further investigate, we fixed the hard PL photon index to the values reported by M. Rigoselli et al. 2025 ($\Gamma_{\rm HPL} = 1.1$ for BB+PL+PL and $\Gamma_{\rm HPL} = 1.3$ for BB+BB+PL). In the BB +PL+PL model, the 6−10 keV absorbed flux of the soft PL is $\sim 1.54 \times 10^{-11}\,{\rm erg\,s^{-1}\,cm^{-2}}$, while the hard PL contributes only $\sim 2.87 \times 10^{-13}\,{\rm erg\,s^{-1}\,cm^{-2}}$, suggesting that its contribution is negligible. In the BB+BB+PL model, however, the hard PL contributes $\sim 5.56 \times 10^{-12}\,{\rm erg\,s^{-1}\,cm^{-2}}$, compared to $\sim 1.01 \times 10^{-11}\,{\rm erg\,s^{-1}\,cm^{-2}}$ from the hotter BB, indicating a more substantial contribution that affects the parameters of the hotter BB. The complete fitting parameters are shown in Table 4.

3.3.1. Phase-averaged Spectral Evolution

We perform the spectral fitting for each observation using the BB+PL model, and the results are shown in Table 1. In Figure 8, the evolution of the BB temperature ($kT_{\rm BB}$), BB radius, photon index of PL, unabsorbed flux in 0.5–10 keV, and proportion of BB component to the total flux with time are displayed from top to bottom panels.

As observed in previous outbursts, the source showed no detectable signs of temporal variation in spectral parameters. In Figure 8(a) and (b), the BB remains approximately stable at $kT_{\rm BB} \sim 0.48$ keV temperature, with an average emitting radius of 4.87 km. This source radius in kilometers was derived based on the distance of 8.5 kpc (W. W. Tian & D. A. Leahy 2008). Conversely, when employing a distance of 5.8 kpc (S. Ranasinghe & D. A. Leahy 2018), the average emitting radius is determined to be 3.32 km. It is important to note that the 8.5 kpc distance has been used consistently in prior studies. To ensure comparability with these earlier works (M. Rigoselli et al. 2025; R. Stewart et al. 2025; G. Younes et al. 2025), we have opted to continue using the 8.5 kpc distance throughout this analysis. Figure 8(c) reveals a mean photon index of 2.03; although the last data point exhibits a slight upward trend, the

[26] BB+PL model: `tbabs*(bbodyrad+powerlaw)`.

[27] BB+BB model: `tbabs*(bbodyrad+bbodyrad)`.

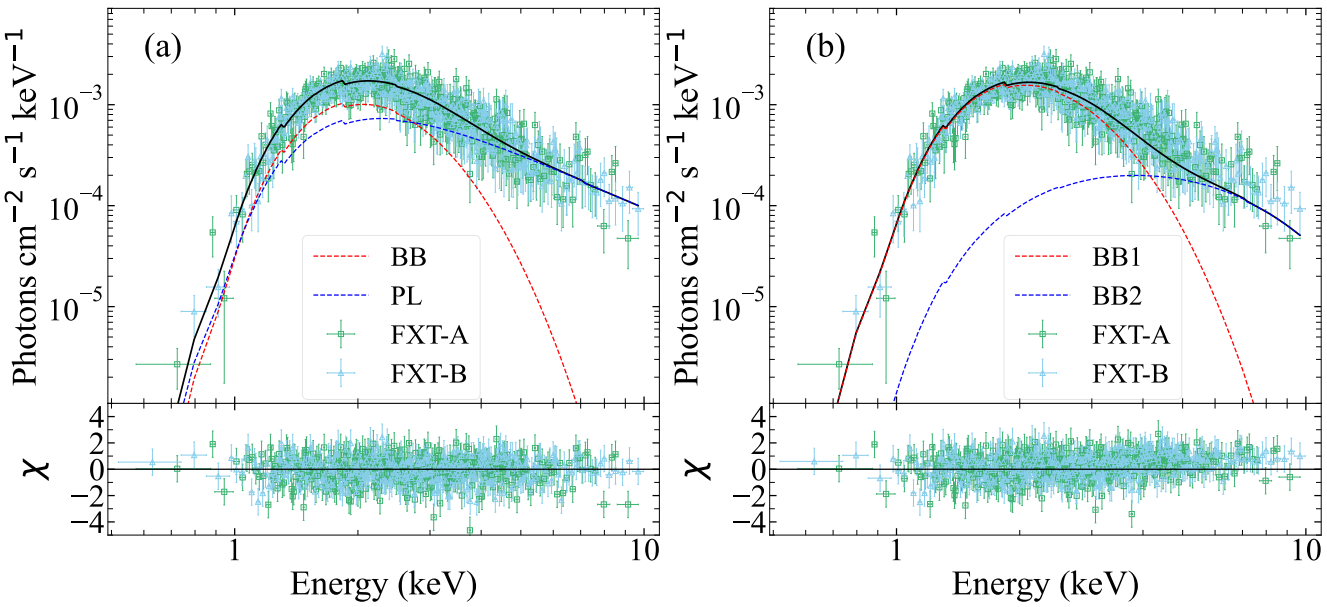

Figure 7. Spectra and residuals from Obs. ID 06800000059. The spectra from FXT-A and FXT-B are extracted separately and fitted jointly. (a) The total model (black solid line) is shown alongside its individual components: a blackbody (red dashed line) and a power-law (blue dashed line). (b) The total model (black solid line) is shown alongside its individual components: a cooler blackbody (red dashed line) and a hotter blackbody (blue dashed line). For clarity, the spectra have been rebinned, and the error bars represent 1σ statistical uncertainties.

large associated uncertainty suggests this deviation is likely due to statistical fluctuations. Due to the limited observation time, the first data point's spectrum lacks sufficient counting statistics, making it unable to effectively constrain the error of the photon index. However, a BB component alone cannot adequately describe the spectrum, so the PL component is still required. Consequently, the photon index of the first point is set at a fixed value of 1.9. The evolution of unabsorbed flux, displayed in Figure 8(d), shows an increase from a preoutburst level of 4.94×10^{-11} erg s^{-1} cm^{-2} to a postoutburst value of $\sim 6 \times 10^{-11}$ erg s^{-1} cm^{-2}, representing a $\sim$20% rise. However, systematic uncertainties from the limited preoutburst sampling (single observation) may affect this estimate. Figure 8(e) presents the BB flux ratio, defined as the unabsorbed BB flux divided by the total unabsorbed flux. The BB ratio exhibits a decrease at the first observation after the outburst.

3.3.2. Phase-resolved Spectral Analysis

In order to analyze the possible transition of the spectral properties of each feature in the pulse profile, we study the phase-resolved spectral analysis. The phase-resolved spectra are modeled well using a BB+PL model combination. Figure 9 presents the phase-resolved spectral fitting results. The gray background traces represent the pulse profile, while the red and blue data points correspond to the BB and PL spectral components, respectively. The horizontal error bars on the data points indicate the phase bin widths used in the analysis. The entire cycle is divided into four phase intervals: peak I (0.85–1.00 phase), peak II (0.05–0.35 phase), peak III (0.40–0.55 phase), and the minimum pulse phase (0.60–0.80 phase). Phase intervals with a low signal-to-noise ratio between the defined peaks were excluded to ensure reliable spectral analysis. The four phase intervals are also indicated by the shaded areas in Figure 5. The fitting yields χ^2/dof ranging from 1.01 to 1.07 across all four phase intervals, with degrees of freedom ranging from 582 to 691.

Our analysis reveals a clear positive correlation between the $kT_{\rm BB}$ of BB and the pulse profile intensity. The BB reaches its maximum temperature value of 0.514 ± 0.007 keV during the main peak (peak II), which corresponds to the highest intensity pulse phase. The temperature gradually decreases in the secondary peak (peak I), with 0.503 ± 0.010 keV. The minor peak (peak III) temperature is even lower at 0.487 ± 0.009 keV. The minimum $kT_{\rm BB}$, which is found to be 0.465 ± 0.008 keV, is observed during the pulse-off phase. In contrast to the $kT_{\rm BB}$ variations, the BB radius remains constant across all pulse phases, showing no statistically significant phase-dependent modulation.

The PL component exhibits complex variability. A constant fit to the four photon index points yields $\Gamma = 1.93 \pm 0.04$ with $\chi^2/{\rm dof} = 3.2/3$, indicating no significant variation in the photon index with phase (horizontal shaded region in Figure 9). The value at peak III ($\Gamma = 1.78 \pm 0.12$) is slightly lower than the constant level, but the deviation is not statistically significant ($\Delta\Gamma = 0.15 \pm 0.13$, corresponding to 1.15σ). The energy-resolved pulse profile analysis (Figure 5) shows that peak III is more prominent at higher energies, which is potentially consistent with a harder spectrum, though the photon index variation itself is not statistically significant. The normalization parameter of the PL component exhibits a potential positive correlation with the pulse profile, reaching its maximum value during the main peak. Fitting the four data points with a constant model yields PL Norm $= 0.017 \pm 0.001$ with a $\chi^2/{\rm dof} = 6.28/3$ ($P = 0.099 > 0.05$), indicating that the data do not significantly deviate from a constant. The peak II point (red area) is marginally elevated, with $\Delta{\rm Norm} = 0.0036 \pm 0.0021$ above the constant level, corresponding to a 1.71σ deviation.

For comparison, we also performed phase-resolved spectral fitting using a BB+BB model, as shown in Figure 10. The fit yields the χ^2/dof for all phase intervals ranging from 1.02 to 1.18, with degrees of freedom ranging from 582 to 691. The

Table 4
EP/FXT Spectral Fitting Results from All Observations of 1E 1841–045

Model	$N_{\rm H}$ (10^{22} cm^{-2})	$kT_{\rm cool}$ (keV)	$R_{\rm cool}$ (km)	$\Gamma_{\rm SPL}$	$kT_{\rm hot}$ (keV)	$R_{\rm hot}$ (km)	$\Gamma_{\rm HPL}$	χ^2/dof
BB+PL	2.08 ± 0.06	0.50 ± 0.01	6.08 ± 0.12	1.91 ± 0.13	…	…	…	754/691
BB+BB	1.73 ± 0.03	0.57 ± 0.01	6.07 ± 0.08	…	2.21 ± 0.08	0.36 ± 0.06	…	803/691
BB+PL+PL	2.08^f	0.55 ± 0.01	5.61 ± 0.37	3.08 ± 0.62	…	…	1.1^f	752/691
BB+BB+PL	1.73^f	0.56 ± 0.01	6.16 ± 0.21	…	1.81 ± 0.24	0.27 ± 0.09	1.3^f	797/691

Note. The source radius in kilometers is calculated from the distance of 8.5 kpc (W. W. Tian & D. A. Leahy 2008). The parameters marked with superscript ^{f} are fixed in the fit.

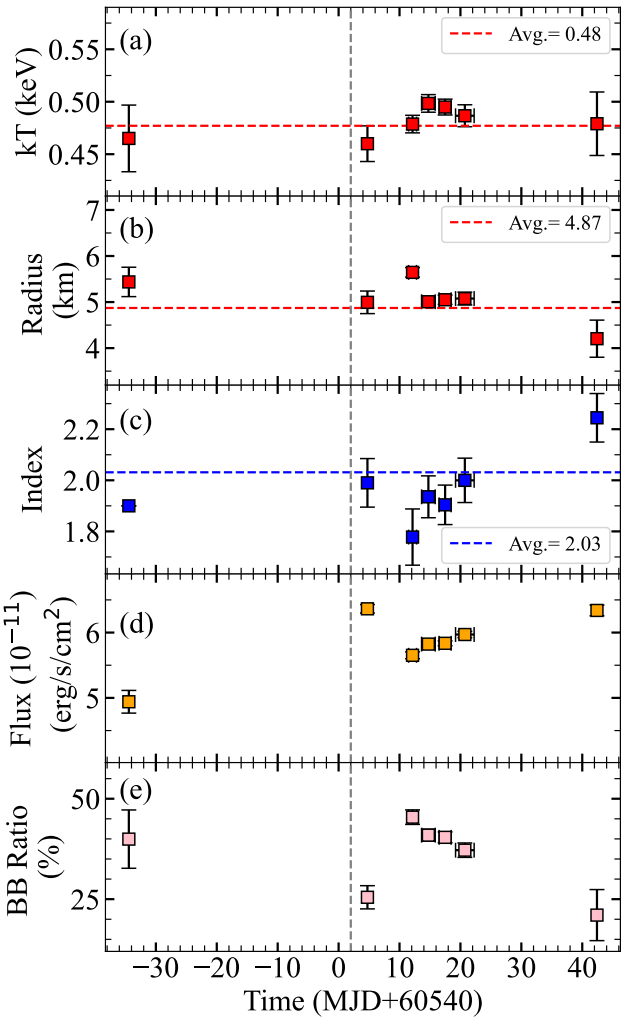

Figure 8. Temporal evolution of spectral parameters: blackbody temperature, emission radius, power-law photon index, unabsorbed total flux, and the fractional contribution of the blackbody flux to the total flux. The source radius in kilometers is calculated from the distance of 8.5 kpc (W. W. Tian & D. A. Leahy 2008). The dashed horizontal line indicates the mean value across all parameters. The dashed vertical line indicates $X = 2$, marking the onset of the outburst. The errors are calculated with 1σ level uncertainties.

cooler BB temperature $kT_{\rm cool}$ exhibits a clear positive correlation with the pulse profile intensity, similar to the behavior observed for the single BB component in the BB+PL model. The radius of the cooler BB remains constant across all phases, showing no significant modulation.

The hotter BB component shows a different behavior. A constant fit to the four $kT_{\rm hot}$ points yields 1.93 ± 0.08 keV with $\chi^2/{\rm dof} = 2.6/3$, indicating no significant variation with phase (horizontal shaded region in Figure 10). The value at peak III slightly increases, though the deviation is not statistically significant ($\Delta kT_{\rm hot} = 0.24 \pm 0.19$ keV, 1.26σ). This behavior is similar to that of the photon index in the BB+PL model, where peak III also showed a marginal hardening. The radius of the hotter BB remains constant within uncertainties across all phases.

3.4. Radio Results

Data processing for FAST in the radio band is conducted on FAST cluster servers, with the main search program based on the single-pulse search module in PRESTO. Based on observations from the Parkes telescope, we set 529 as the reference dispersion measure (DM) value for data analysis of this source and established a search range of 400–600 (step size is 0.04) for DM. Preliminary search results were filtered using a signal-to-noise ratio threshold of 6. The filtered results indicate no significant signal from 1E 1841–045 within the DM range of 400–600 at 1–1.5 GHz. The upper limit for single-pulse flux density is 2.6 mJy across the range of pulse timescales 0.05–50 ms, which is consistent with the upper limits derived for magnetars from J. Bai et al. (2025) and L. Lin et al. (2020).

4. Discussion

We have analyzed the EP observations of 1E 1841–045 during its 2024 active period and performed the timing and spectral analysis of the X-ray persistent emission. The main results are as follows:

1. During the decay of the outburst, we detected a stable spin period of 0.084699564(6) Hz, with a derivative of $-3.04(5) \times 10^{-13}$ Hz s^{-1}, as shown in Table 3.
2. The pulse profile exhibited a multipeaked structure. The secondary peak (peak I) underwent a phase shift of ∼0.1 cycle, while the minor peak (peak III) appeared and disappeared intermittently. The energy-resolved pulse profile revealed a stable triple-peaked structure, with the minor peak becoming significantly enhanced above 5.8 keV, as illustrated in Figures 4 and 5. Moreover, the PF of the integrated pulse profile increased linearly with energy, as depicted in Figure 6.
3. The phase-averaged spectra were well fitted by an absorbed BB+PL model, showing a ∼20% flux increase in the soft (0.5–10 keV) X-ray band following the outburst, as shown in Figures 7 and 8.
4. Phase-resolved analysis indicated a positive correlation between the blackbody temperature ($kT_{\rm BB}$) and the pulse profile intensity, with $kT_{\rm BB}$ tracing the pulse profile.

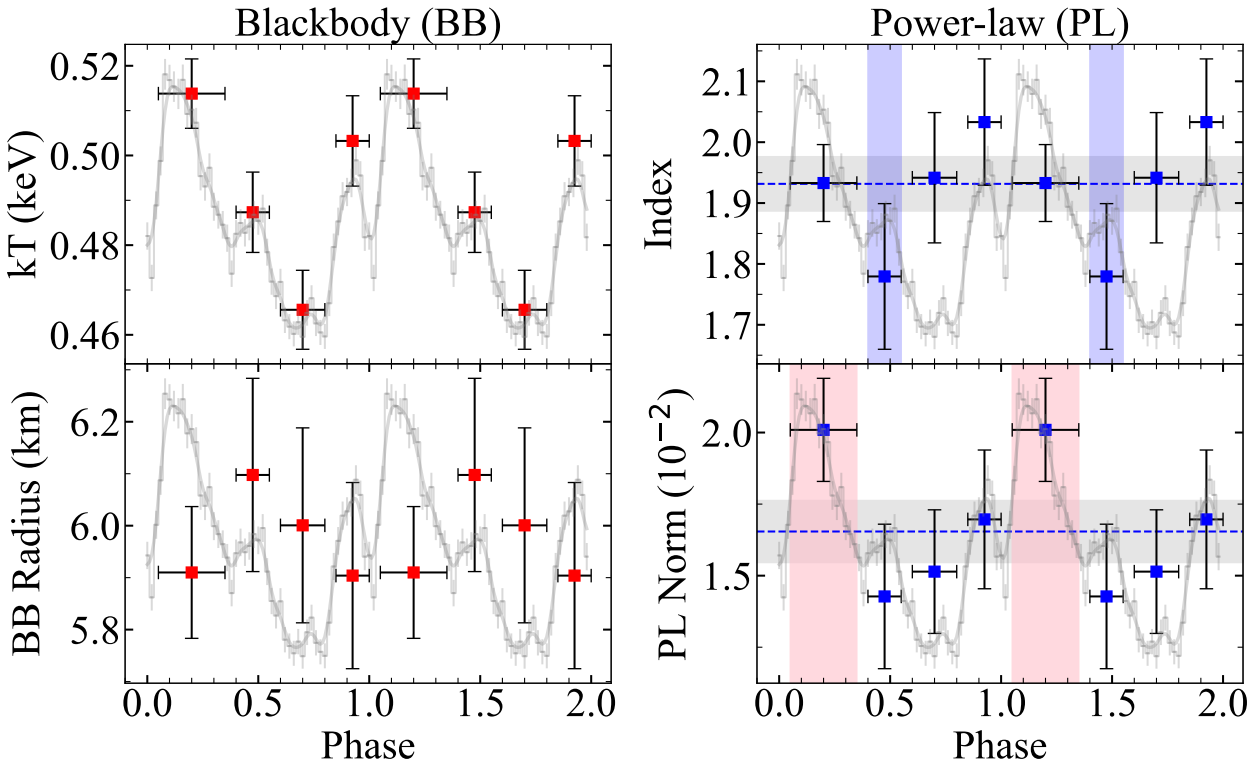

Figure 9. Fitting results of the phase-resolved spectral analysis of the BB+PL model. Solid lines represent the pulse profiles as shown in Figure 3 (epoch II). The blue dashed horizontal lines represent the constant fits for the photon index ($\Gamma = 1.93 \pm 0.04$) and the PL normalization (0.017 ± 0.001), with gray shaded 1σ uncertainties. The blue and pink vertical bands mark peak III and the main peak (peak II), respectively. The source radius in kilometers is calculated from the distance of 8.5 kpc (W. W. Tian & D. A. Leahy 2008). The errors are calculated with 1σ level uncertainties.

Additionally, there was spectral hardening of the PL component at the minor peak, as shown in Figure 9.

4.1. Timing and Pulse Profile

The occurrence of spin-up glitches during the onset of outburst is well documented in the persistently monitored X-ray magnetars (R. Dib & V. M. Kaspi 2014), just like the glitch observed in 1E 1841–045 at the 2024 outburst monitored by NICER (G. Younes et al. 2025). The spin-up glitches are typically explained by the superfluid mechanism in pulsars, where angular momentum is transferred from the faster-rotating superfluid component in the NS's inner crust to the slower-rotating outer crust that is being braked by magnetic dipole radiation (e.g., A. Lyne & F. Graham-Smith 2012). For 1E 1841–045, the initial FXT ToO observation was conducted on MJD 60544.74, approximately 1.74 days later than the reported glitch epoch (MJD 60543; G. Younes et al. 2025). Due to the limited preglitch coverage consisting of only one brief monitoring observation, FXT's observational gap prevented the detection of this glitch event. This underscores the need for continuous monitoring during outburst onset.

Before and after the outburst, there was a significant change in the pulse profile shape, as shown in Figure 3. The preoutburst bimodal structure evolved into a triple-peaked profile, with the strongest main peak splitting into two components and the newly emerged secondary peak (peak I) displaying a phase width of approximately 0.15. The smallest minor peak (peak III) exhibited no detectable variation. This pulse profile evolution was also independently detected by NICER observations (G. Younes et al. 2025). Following the outburst, FXT similarly detected a phase shift in the newly emerged peak, which exhibited gradual rightward drift toward the main peak, suggesting an eventual merging trend. FXT's monitoring duration was substantially shorter than NICER's and insufficient for deriving quantitative drift measurements. However, we obtained a crude estimate of $\sim 2.6 \times 10^{-3}$ cycle day^{-1}. This value exceeds NICER's precise measurement of $7.3(5) \times 10^{-4}$ cycle day^{-1} (G. Younes et al. 2025), yet we contend that FXT independently corroborates NICER's findings.

The pulse profile also exhibits significant variability across different energy bands. Historical records indicate that 1E 1841–045 shows a flatter pulse profile in hard X-rays (e.g., L. Kuiper et al. 2004; H. An et al. 2013). RXTE observations revealed a transition in the main pulse structure when energy exceeded ~ 9 keV, with the dominant peak moving from phase $\sim$0.3 to phase $\sim$0.7 (L. Kuiper et al. 2004). NuSTAR detected the same transition phenomenon, though occurring at a higher energy boundary at $\sim$11 keV. Considering the measurement uncertainties, the difference between $\sim$9 keV and $\sim$11 keV was insignificant (H. An et al. 2013). During the 2024 outburst, NuSTAR observations demonstrated that while the 10–20 keV profile was dominated by a peak at phase $\sim$0.75, the 3–10 keV profile was dominated by a peak at phase $\sim$0.5. In contrast to historical records, the previously observed peak at phase $\sim$0.3 split into two narrower peaks at phases $\sim$0.2 and $\sim$0.5 (G. Younes et al. 2025). FXT provided higher energy-resolution pulse profiles in the 0.5–10 keV soft X-ray band, clearly showing that the dominant peak transition occurred at $\sim$5.8 keV (see Figure 5). Above this threshold energy, the primary peak dominance transitioned from peak II (corresponding to phase $\sim$0.5 of NuSTAR mentioned earlier) to peak

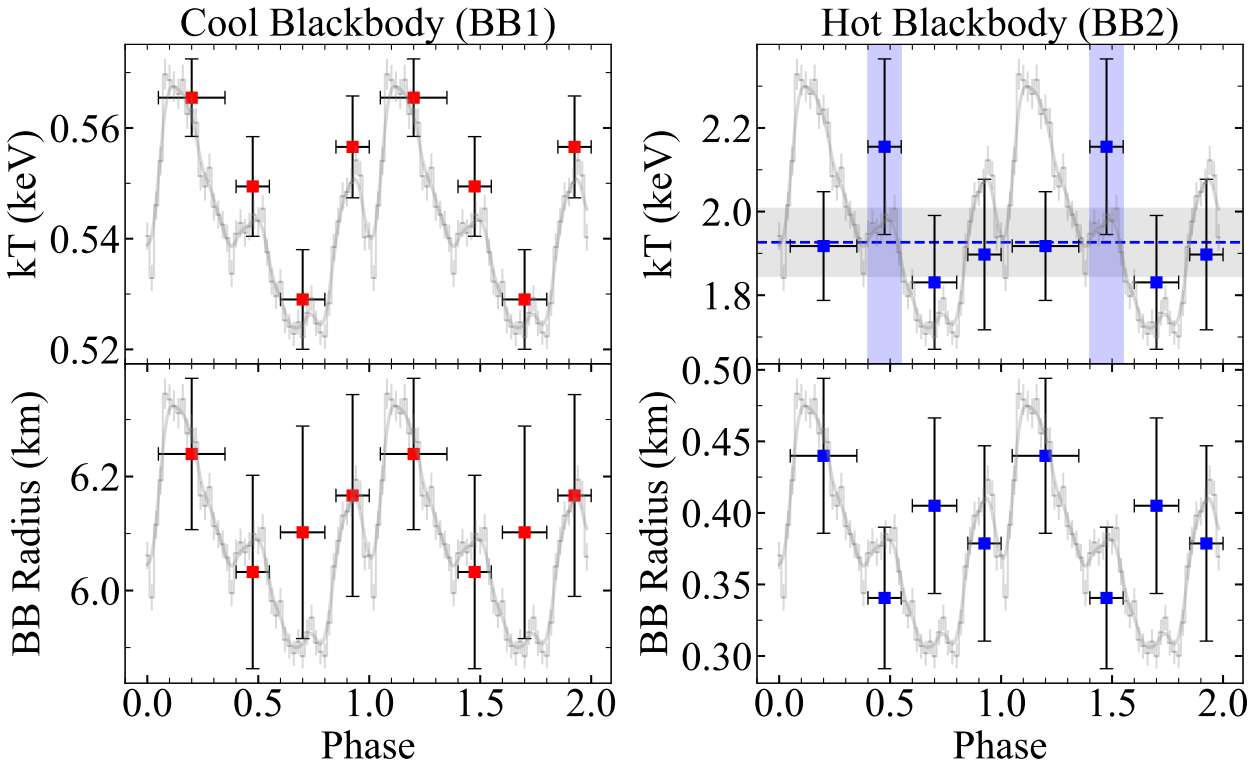

Figure 10. Fitting results of the phase-resolved spectral analysis of the BB+BB model. The blue dashed horizontal line indicates the constant fit result for the hotter BB temperature (1.93 ± 0.08 keV), with the gray shaded region representing the 1σ uncertainty. The blue vertical band highlights the phase interval corresponding to peak III. The source radius in kilometers is calculated from the distance of 8.5 kpc (W. W. Tian & D. A. Leahy 2008). The errors are calculated with 1σ level uncertainties.

III (corresponding to phase ∼0.75). The discrepancy between ∼5.8 keV and the historically recorded ∼9 keV or ∼11 keV should not be overlooked, and it suggests potential changes in the energy boundary for pulse profile transitions. This energy boundary has been associated with the spectral break (H. An et al. 2013). FXT's spectral analysis showed no other notable changes beyond ∼5.8 keV except for the increasing dominance of the PL component. The phase-resolved spectra also indicate that peak III has a potentially harder spectrum than other phase intervals. This indicates that peak III originated from a different location than peaks I and II.

The PF demonstrates minimal temporal variability, as evidenced by the FXT mean PF remaining constant at 23.4% ± 2.9%. Both NuSTAR and NICER observations exhibit a similar steady trend, but the derived PF values are ∼11% and ∼6%, respectively (G. Younes et al. 2025), which are lower than the PF value of FXT. IXPE measurements reveal a PF of 21.2% ± 1.5% in the 2–4 keV energy band and 27.6% ± 7.3% in the 4–8 keV energy band. While a slight increase in PF at higher energies is observed, this trend lacks strong statistical significance, suggesting minimal energy dependence in the IXPE energy range (M. Rigoselli et al. 2025; R. Stewart et al. 2025). In contrast, in previous observations of the source, the PF for 1E 1841–045 exhibited an energy-dependent increase across broad energy bands. According to L. Kuiper et al. (2006), the PF reaches ∼25% at 20 keV, increasing to nearly 100% at energies above 100 keV. H. An et al. (2013) also reported an increase in PF from 10% at 2 keV to 20% at 80 keV. During the 2024 outburst, FXT's soft X-ray measurements show that the PF exhibits an increasing trend with energy below ∼5 keV, rising from ∼15% at ∼0.5 keV to ∼25% at ∼5 keV, with a linear growth rate of 2.8% ± 0.9% per keV. Beyond ∼5 keV, the behavior is poorly constrained due to large uncertainties.

4.2. Soft X-Ray Spectra

The 0.5–79 keV X-ray spectrum of 1E 1841–045 shows some variability in the fitting results (e.g., L. Kuiper et al. 2004; M. Morii et al. 2010; S.-S. Weng & E. Göğüş 2015). The previous fitting results indicate the spectrum above 3 keV is dominated by a nonthermal component, and in this case, a model with two PL components can fit the 3–79 keV spectrum (T. Enoto et al. 2017; G. Younes et al. 2025). After the outburst, the increased soft component makes the thermal component more significant in the model. For the soft 0.5–10 keV spectrum, the BB+PL combination provides a good fit, with Swift, XMM-Newton, and Chandra observations giving a typical BB temperature of ∼0.46 keV and a PL photon index ranging from 1.76 to 2.07 (H. An et al. 2013). The best-fit results from FXT's 0.5–10 keV spectra show the typical BB temperature is 0.50 ± 0.01 keV, and the PL photon index is 1.71 ± 0.13, which shows good agreement with the Swift measurements. The FXT freely fitted $N_{\rm H}$ value of $(2.08 \pm 0.06) \times 10^{22}\,{\rm cm}^{-2}$ is slightly lower than Swift's fitted value of $(2.23 \pm 0.25) \times 10^{22}\,{\rm cm}^{-2}$ (H. An et al. 2013). Other analyses also provided different measurement values between $\sim$(2.4 and 2.9) $\times 10^{22}\,{\rm cm}^{-2}$ (L. Lin et al. 2011; H. An et al. 2013; T. Enoto et al. 2017; M. Rigoselli et al. 2025; R. Stewart et al. 2025). However, when considering factors such as instrumental differences, varying activity periods, and efficiency corrections for Kes 73's influence, this discrepancy may be negligible.

1E 1841–045 showed almost no significant changes in its spectral parameters following the outburst, with the soft X-ray flux increasing by ∼20% compared to preoutburst levels. In the case of another active magnetar, SGR J1935+2154 (G. Younes et al. 2020; Y.-C. Fu et al. 2025), the decay pattern revealed that the BB and PL components did not decrease in tandem during the outburst decay. The BB component rapidly weakened within a few hours, while the PL component decayed slowly over several days. Eventually, the source entered a relatively stable phase characterized by constant spectral parameters. The persistent emission outburst of SGR J1935+2154 was more intense than that of 1E 1841–045, resulting in more discernible differences in the decay of thermal and nonthermal spectral components. Specifically, the BB flux ratio increased from ∼10% during the outburst to ∼60% in the quiescent state (Y.-C. Fu et al. 2025). We attempted to track the evolution of the BB and PL components in 1E 1841–045. Before the outburst, the BB flux fraction was ∼40%, which dropped to ∼25% postoutburst, and then eventually recovered to ∼40%. However, due to sparse observational coverage, a definitive picture of the BB ratio evolution could not be established. Nevertheless, when compared to SGR J1935+2154, the weaker outburst activity of 1E 1841–045, along with its less pronounced BB ratio evolution, appears to be in harmony.

Previous studies have discussed the emission mechanisms of 1E 1841–045's pulsed emission (H. An et al. 2013, 2015; G. Younes et al. 2025). Regardless of whether it is explained by the "outflow" model (A. M. Beloborodov 2009; A. M. Beloborodov 2013) or the "plastic motions" model (C. Thompson et al. 2002; G. Younes et al. 2025), the emission is thought to be of nonthermal origin. The soft X-ray emission originates from hot spots generated by high-energy charged particles bombarding the NS's surface, such as the footpoints of twisted magnetic field lines (A. M. Beloborodov & X. Li 2016). Meanwhile, the nonthermal emission in the high-energy band can extend below 10 keV (H. An et al. 2013). Thus, a single BB component cannot adequately fit the 0.5–10 keV spectrum. Instead, an additional component is required, and either a BB +BB model (accounting for multiple thermal components) or a BB+PL model (combining thermal and nonthermal emission) can be employed to achieve a better fit. The evolution of the low-temperature BB ratio actually reflects the heating process of the hot spots by high-energy charged particles.

The phase-resolved spectra of the soft X-ray emission do not fully agree with the results reported by H. An et al. (2013). A distinct positive correlation is observed between BB temperature and the intensity of the pulse profile. This marks the first detection of significant phase-dependent variations in the BB component of this source. The photon index of the PL component remains relatively stable across different phases, except for a slightly harder spectrum observed at peak III of the pulse profile. This finding is further supported by the energy-resolved pulse profile analysis. Notably, NuSTAR's phase-resolved spectroscopy reveals the same trend. A single PL component provides an excellent fit to the hard X-ray pulse-phase spectra, and it exhibits a harder energy spectrum at the third peak (G. Younes et al. 2025). This implies that the PL component in the soft X-ray energy range exhibits the same behavior as the PL component in the hard X-ray energy range. This consistency may indicate a common nonthermal origin for the pulsed emission across the two energy bands. Therefore, from a physical standpoint, these results indicate that the BB+PL model may provide a more suitable description of the soft X-ray spectra than the BB+BB model, though the current data cannot statistically distinguish between the two models. The normalization of the PL component is consistent with a constant within uncertainties. However, a slight excess is observed at peak II ($\Delta\mathrm{Norm} = 0.0036 \pm 0.0021$, corresponding to a 1.71σ deviation), but its statistical significance is marginal. Given this marginal significance, deeper observations are needed to confirm whether this excess reflects a genuine nonthermal contribution to the pulsed emission. The spatial resolution of EP offers a significant advantage over instruments like NICER, particularly for analyzing sources located within the circular ring of SNR. Although the separability of the SNR has a relatively minor impact (∼2%) on the calculation of the source's PF in 1E 1841–045, it still helps to mitigate any adverse effects from the surrounding region. More crucially, the SNR exerts a substantial influence on the spectral fitting of the source. Therefore, separating the SNR emission in the soft X-ray band is important for accurately measuring the neutral hydrogen column density (N_{H}) toward the source.

Acknowledgments

This work has made use of data from the EP mission, as well as data and software provided by the Einstein Probe Science Center (EPSC). This work is also based on data obtained by Insight-HXMT, NICER, Swift, and FAST missions. This work is supported by the National Key R&D Program of China (2021YFA0718504). The authors thank support from the National Natural Science Foundation of China under grants U2038103, U2038101, U2038102 and 12373051. This work is also supported by International Partnership Program of Chinese Academy of Sciences (grant No.113111KYSB20190020). F.C.Z. is supported by a Ramón y Cajal fellowship (grant agreement RYC2021-030888-I), the Spanish grant ID2023-153099NA-I00, and the program Unidad de Excelencia Maria de Maeztu CEX2020-001058-M. We would like to thank Dr. George Younes for his helpful comments and suggestions on this project. We also thank the anonymous referee for the insightful comments and suggestions that improved the quality of this work.

Software: ASTROPY (Astropy Collaboration et al. 2013, 2018), XSPEC (K. A. Arnaud 1996), and STINGRAY (D. Huppenkothen et al. 2019).

ORCID iDs

Yu-Cong Fu https://orcid.org/0009-0005-2228-0618
Lin Lin https://orcid.org/0000-0002-0633-5325
Ming-Yu Ge https://orcid.org/0000-0002-2749-6638
Han-Long Peng https://orcid.org/0009-0009-8477-8744
Francesco Coti Zelati https://orcid.org/0000-0001-7611-1581
Ersin Göğüş https://orcid.org/0000-0002-5274-6790
Nanda Rea https://orcid.org/0000-0003-2177-6388
Bing Zhang https://orcid.org/0000-0002-9725-2524
Wei-Wei Zhu https://orcid.org/0000-0001-5105-4058
Teruaki Enoto https://orcid.org/0000-0003-1244-3100
Chryssa Kouveliotou https://orcid.org/0000-0003-1443-593X

References

An, H., Archibald, R. F., Hascoët, R., et al. 2015, ApJ, 807, 93
An, H., Hascoët, R., Kaspi, V. M., et al. 2013, ApJ, 779, 163
Archibald, R. F., Kaspi, V. M., Ng, C.-Y., et al. 2013, Natur, 497, 591
Arnaud, K. A. 1996, ASPC, 101, 17
Astropy Collaboration, Price-Whelan, A. M., Sipőcz, B. M., et al. 2018, AJ, 156, 123
Astropy Collaboration, Robitaille, T. P., Tollerud, E. J., et al. 2013, A&A, 558, A33
Bai, J., Wang, N., Dai, S., et al. 2025, ApJ, 979, 122
Beloborodov, A. M. 2009, ApJ, 703, 1044
Beloborodov, A. M. 2013, ApJ, 762, 13
Beloborodov, A. M., & Li, X. 2016, ApJ, 833, 261
Borghese, A., Coti Zelati, F., Rea, N., et al. 2020, ApJL, 902, L2
Burgay, M., Rea, N., Israel, G. L., et al. 2006, MNRAS, 372, 410
Cai, C., Li, X.-B., Xiong, S.-L., et al. 2024, GCN, 37606, 1
Chen, Y., Cui, W., Han, D., et al. 2020, SPIE, 11444, 114445B
Coti Zelati, F., Rea, N., Pons, J. A., Campana, S., & Esposito, P. 2018, MNRAS, 474, 961
DeLaunay, J. J., Dichiara, S., Lien, A. Y., Parsotan, T. M. & Neil Gehrels Swift Observatory TeamObservatory Team 2024, GCN, 37211, 1
Dib, R., & Kaspi, V. M. 2014, ApJ, 784, 37
Dichiara, S., Palmer, D. M. & Neil Gehrels Swift Observatory TeamObservatory Team 2024, GCN, 37222, 1
Duncan, R. C., & Thompson, C. 1992, ApJL, 392, L9
Edwards, R. T., Hobbs, G. B., & Manchester, R. N. 2006, MNRAS, 372, 1549
Enoto, T., Shibata, S., Kitaguchi, T., et al. 2017, ApJS, 231, 8
Fu, Y.-C., Lin, L., Ge, M.-Y., et al. 2025, ApJ, 980, 99
Fu, Y.-C., Song, L. M., Ding, G. Q., et al. 2023, MNRAS, 521, 893
Gavriil, F. P., Kaspi, V. M., & Woods, P. M. 2004, ApJ, 607, 959
Ge, M. Y., Lu, F. J., Qu, J. L., et al. 2012, ApJS, 199, 32
Ge, M. Y., Lu, F. J., Yan, L. L., et al. 2019, NatAs, 3, 1122
Ge, M.-Y., Yang, Y.-P., Lu, F.-J., et al. 2024, RAA, 24, 015016
Gotthelf, E. V., Vasisht, G., & Dotani, T. 1999, ApJL, 522, L49
Huppenkothen, D., Bachetti, M., Stevens, A. L., et al. 2019, ApJ, 881, 39
Jiang, P., Tang, N.-Y., Hou, L.-G., et al. 2020, RAA, 20, 064
Kouveliotou, C., Dieters, S., Strohmayer, T., et al. 1998, Natur, 393, 235
Kriss, G. A., Becker, R. H., Helfand, D. J., & Canizares, C. R. 1985, ApJ, 288, 703
Kuiper, L., Hermsen, W., den Hartog, P. R., & Collmar, W. 2006, ApJ, 645, 556
Kuiper, L., Hermsen, W., & Mendez, M. 2004, ApJ, 613, 1173
Lazarus, P., Kaspi, V. M., Champion, D. J., Hessels, J. W. T., & Dib, R. 2012, ApJ, 744, 97
Leahy, D. A. 1987, A&A, 180, 275
Lin, L., Kouveliotou, C., Göğüş, E., et al. 2011, ApJL, 740, L16
Lin, L., Zhang, C. F., Wang, P., et al. 2020, Natur, 587, 63
Liu, Y., Sun, H., Xu, D., et al. 2025, NatAs,
Lyne, A., & Graham-Smith, F. 2012, Pulsar Astronomy (Cambridge Univ. Press)
Lyutikov, M., & Gavriil, F. P. 2006, MNRAS, 368, 690
Mereghetti, S., Gotz, D., Ferrigno, C., et al. 2024, GCN, 38148, 1
Mereghetti, S., Pons, J. A., & Melatos, A. 2015, SSRv, 191, 315
Morii, M., Kitamoto, S., Shibazaki, N., et al. 2010, PASJ, 62, 1249
Ng, M., Younes, G., Hu, C. P., et al. 2024, ATel, 16789, 1
Olausen, S. A., & Kaspi, V. M. 2014, ApJS, 212, 6
Peng, H.-L., Weng, S.-S., Ge, M.-Y., et al. 2026, ApJ, 999, 85
Ranasinghe, S., & Leahy, D. A. 2018, AJ, 155, 204
Rea, N., & De Grandis, D. 2026, Encyclopedia of Astrophysics, 3, 205
Rigoselli, M., Taverna, R., Mereghetti, S., et al. 2025, ApJL, 985, L34
Roberts, O. J., Veres, P., de Barra, C., et al. 2024, GCN, 37234, 1
Stewart, R., Younes, G. A., Harding, A. K., et al. 2025, ApJL, 985, L35
SVOM/GRM Team, Wang, C.-W., Dong, Y.-W., et al. 2024a, GCN, 37297, 1
SVOM/GRM Team, Zhang, W.-L., Tan, W.-J., et al. 2024b, GCN, 38192, 1
Thompson, C., & Duncan, R. C. 1993, ApJ, 408, 194
Thompson, C., Lyutikov, M., & Kulkarni, S. R. 2002, ApJ, 574, 332
Tian, W. W., & Leahy, D. A. 2008, ApJ, 677, 292
Tong, H., Xu, R.-X., Peng, Q.-H., & Song, L.-M. 2010, RAA, 10, 553
Vasisht, G., & Gotthelf, E. V. 1997, ApJL, 486, L129
Weng, S.-S., & Göğüş, E. 2015, ApJ, 815, 15
Woods, P. M., Kaspi, V. M., Thompson, C., et al. 2004, ApJ, 605, 378
Yin, Y.-H. I., Zhang, B.-B., Yang, J., et al. 2024, ApJL, 975, L27
Younes, G., Baring, M. G., Kouveliotou, C., et al. 2017a, ApJ, 851, 17
Younes, G., Güver, T., Kouveliotou, C., et al. 2020, ApJL, 904, L21
Younes, G., Hu, C. P., Enoto, T., et al. 2024, ATel, 16802, 1
Younes, G., Kouveliotou, C., Jaodand, A., et al. 2017b, ApJ, 847, 85
Younes, G., Lander, S. K., Baring, M. G., et al. 2025, ApJ, 989, 89
Yuan, W., Dai, L., Feng, H., et al. 2025, SCPMA, 68, 239501
Yuan, W., Zhang, C., Chen, Y., & Ling, Z. 2022, in Handbook of X-ray and Gamma-ray Astrophysics, ed. C. Bambi & A. Sangangelo (Springer), 86
Zhang, W., Yuan, W., Ling, Z., et al. 2025, SCPMA, 68, 219511
Zhang, W.-L., Xiong, S.-L., Tan, W.-J., Huang, Y., & Team, G. 2024, GCN, 37240, 1
Zhu, W., & Kaspi, V. M. 2010, ApJ, 719, 351